AGU PUBLICATIONS

JGR

Journal of Geophysical Research: Space Physics

RESEARCH ARTICLE
10.1002/2016JA022659

Key Points:
- Significant difference in the low-latitude E_s characteristics has been observed in the concurrent and drifted ESF events
- Model computation indicates that the E_s in the low latitudes can generate LSWS
- LSWS linked with low-latitude E_s alters the collisional R-T instability growth rate as well as its efficiency

Correspondence to:
L. M. Joshi,
lmjoshinarl@gmail.com

Citation:
Joshi, L. M. (2016), LSWS linked with the low-latitude E_s and its implications for the growth of the R-T instability, *J. Geophys. Res. Space Physics*, *121*, doi:10.1002/2016JA022659.

Received 4 MAR 2016
Accepted 29 JUN 2016
Accepted article online 2 JUL 2016

LSWS linked with the low-latitude E_s and its implications for the growth of the R-T instability

L. M. Joshi[1]

[1]Indian Institute of Geomagnetism, Navi Mumbai, India

Abstract A comprehensive investigation of spread *F* irregularities over the Indian sector has been carried out using VHF radar and ionosonde observations. Two different categories of spread *F* observations, one where the onset of the range spread *F* (RSF) was concurrent with the peak *h'F* (category 1) and another where the RSF onset happened ~90 min after the peak *h'F* time (category 2), are presented. RSF in category 2 was preceded by the presence of oblique echoes in ionograms, indicating the irregularity genesis westward of Sriharikota. The average peak *h'F* in category 1 was ~30 km higher than that in category 2 indicating the presence of standing large-scale wave structure (LSWS). Occurrence of the blanketing E_s during 19:30 to 20:30 Indian Standard Time in category 1 (category 2) was 0% (>50%). Model computation is also carried out to further substantiate the observational results. Model computation indicates that zonal variation of low-latitude E_s can generate zonal modulation in the *F* layer height rise. It is found that the modulation of the *F* layer height, linked with the low-latitude E_s, assists the equatorial spread *F* onset by modifying both the growth rate of the collisional Rayleigh-Taylor (R-T) instability and also its efficiency. A predominant presence of low-latitude E_s has been observed, but the increase in the *F* layer height and the R-T instability growth in the evening hours will maximize with complete absence of low-latitude E_s. A new mechanism for the generation of LSWS and its implications on R-T instability is discussed.

1. Introduction

Equatorial spread *F* (ESF) has been a subject of extensive scientific research, worldwide, for over seven decades. Still it has not been fully resolved. The most puzzling aspect of the ESF is its day-to-day variability. Prediction of the ESF on a day-to-day basis has been and still continues to be a challenge for the researchers. ESF is broadly characterized into two types, the bottomside/bottom-type spread *F* and the topside spread *F* [*Woodman and LaHoz*, 1976; *Hysell and Burcham*, 1998]. The bottomside/bottom-type spread *F* is associated with the ionospheric irregularities confined to the bottomside *F* region, and it does not affect the satellite-based navigation and communication, while the topside spread *F* is associated with the generation of equatorial plasma bubbles (EPBs), which could have an altitudinal (latitudinal) extent of more than a thousand kilometers (±15°) [*Hysell et al*., 1990]. EPBs are generated due to plasma interchange process at the bottom of the *F* layer [*Zalesak and Ossakow*, 1980]. Topside spread *F* can significantly influence the availability and also the accuracy of satellite-based navigation systems. Topside spread *F* is often preceded by the bottom-type spread *F* [*Hysell et al*., 2004].

Various investigations have revealed the presence of large-scale longitudinal modulation of the ESF [eg., *Kelley et al*., 1981; *Tsunoda*, 1983]. It has been found that the equatorial plasma bubble does not occur continuously but has a longitudinal modulation much greater than the longitudinal dimension of an individual bubble [*Tsunoda et al*., 2011; *Tulasi Ram et al*., 2012; *Li et al*., 2013; *Tulasi Ram et al*., 2014; *Tsunoda*, 2015; *Li et al*., 2016]. This longitudinal modulation has been found to be related with the large-scale wave structure (LSWS) found in the evening *F* layer. Studies have established the LSWS as one of the important precursors for the generation of the EPB. One of the interesting facts about the LSWS is the absence of a significant longitudinal propagation [*Tsunoda and Ecklund*, 2007; *Joshi et al*., 2015]. LSWS evolves as standing wave with insignificant zonal propagation. Plasma bubbles usually occur at the crest and the westward face of the large-scale upwelling [*Tsunoda*, 1983]. Wind-driven cross field instability has been accounted for the bubble initiation on the westward wall of the large-scale upwelling by *Tsunoda* [1983]. That being the case, the LSWS turns out to be an important if not the only precondition for the onset of the ESF. LSWS has been studied using a variety of tools which includes coherent scatter radar [e.g., *Tsunoda and Ecklund*, 2007], incoherent scatter radar [*Tsunoda and White*, 1981], ionosonde [*Tsunoda*, 2008, 2009; *Lynn et al*., 2011; *Li et al*., 2012],

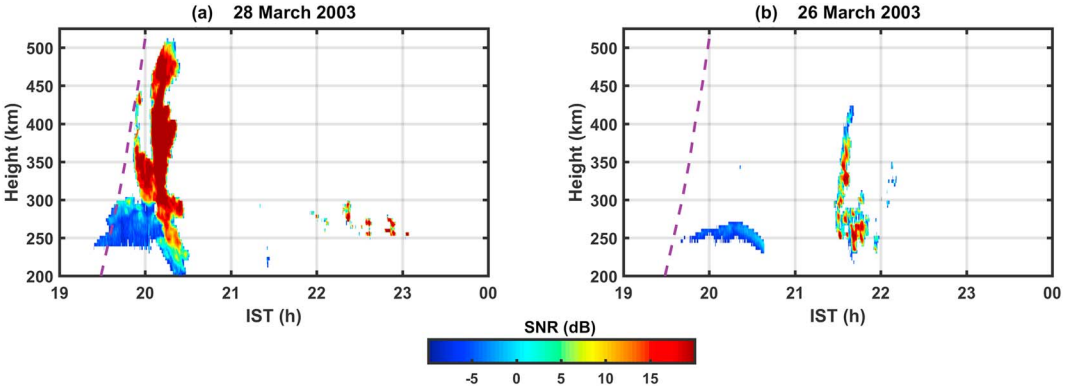

Figure 1. Height-time-SNR map of Gadanki VHF radar on (a) 28 March 2003 and (b) 26 March 2003.

and satellite in situ [*Huang et al*., 2013] and beacon measurements [*Thampi et al*., 2009]. Satellite traces as well as multireflected echo traces in the ionogram have been considered as important indicators of the LSWS, while there have also been some studies which have highlighted the appearance of LSWS in the airglow instruments with no satellite trace being observed in the ionosonde [*Patra et al*., 2013].

While a lot of studies have highlighted the presence of a longitudinal modulation in the occurrence of the ESF, still not much is known about the cause of such features. Two of the important issues that need to be further resolved are the following: (1) what is the mechanism for the generation of the large-scale waves and thus the longitudinal variation of the ESF and (2) what is the role of such large-scale waves in the generation of the plasma bubbles and the onset of the ESF?

This paper presents two different categories of spread *F* events observed using an ionosonde, one where the onset of spread *F* is concurrent with the peak *h*′*F* (category 1) and another where the spread *F* onset happened after more than an hour with respect to the peak *h*′*F* time (category 2). Considering the genesis of the EPB to happen at or before the time of the *F* layer attaining the peak height, late onset of ESF indicates the genesis of the EPB to have happened at a western longitude (considering eastward drifting ionosphere). This aspect will be discussed in details in the paper. It will be shown that the peak *h*′*F* is significantly higher in category 1 than in category 2, which indicates a possible presence of LSWS. Based on model computation, a new mechanism for the generation of LSWS and its implication on the growth of the Rayleigh-Taylor (R-T) instability will be proposed.

2. Observational Data

The study presented in this paper has been carried out, utilizing the VHF radar and ionosonde observations from Gadanki (13.5°N, 79.2°E, 6.5°N magnetic latitude) and Sriharikota (13.7°N, 80.1°E, 6.7°N magnetic latitude), respectively. Both Gadanki and Sriharikota are low-latitude stations in India, separated by 100 km. VHF radar located at Gadanki has been used to observe the nature of the *F* region irregularity and to compare it with spread *F* observation over Sriharikota. Observations made during the equinox period have only been considered for the study.

3. Results and Discussion

3.1. Coordinated VHF Radar and Ionosonde Observations of *F* Region Irregularities

Figures 1a and 1b show the height-time-SNR (HTS) plot of Gadanki VHF radar observation on 28 March 2003 and 26 March 2003, respectively. On both the nights, radar plumes indicating the occurrence of EPBs were observed. Dashed purple curve in the plots indicates the sunset terminator. On 28 March the radar plumes were observed close to the *F* region sunset time with no irregularities observed between 20:30 IST and 22:00 IST (here IST stands for Indian Standard Time UT + 5:30). Between 22:00 IST and 23:00 IST some radar echoes were detected which were confined between the height range 250 to 300 km. Radar observation on 26 March differed significantly with the former in the sense that the radar plume was not observed around the *F* region sunset time. The HTS plot for 26 March shows the observation of radar plume at ~21:30 IST.

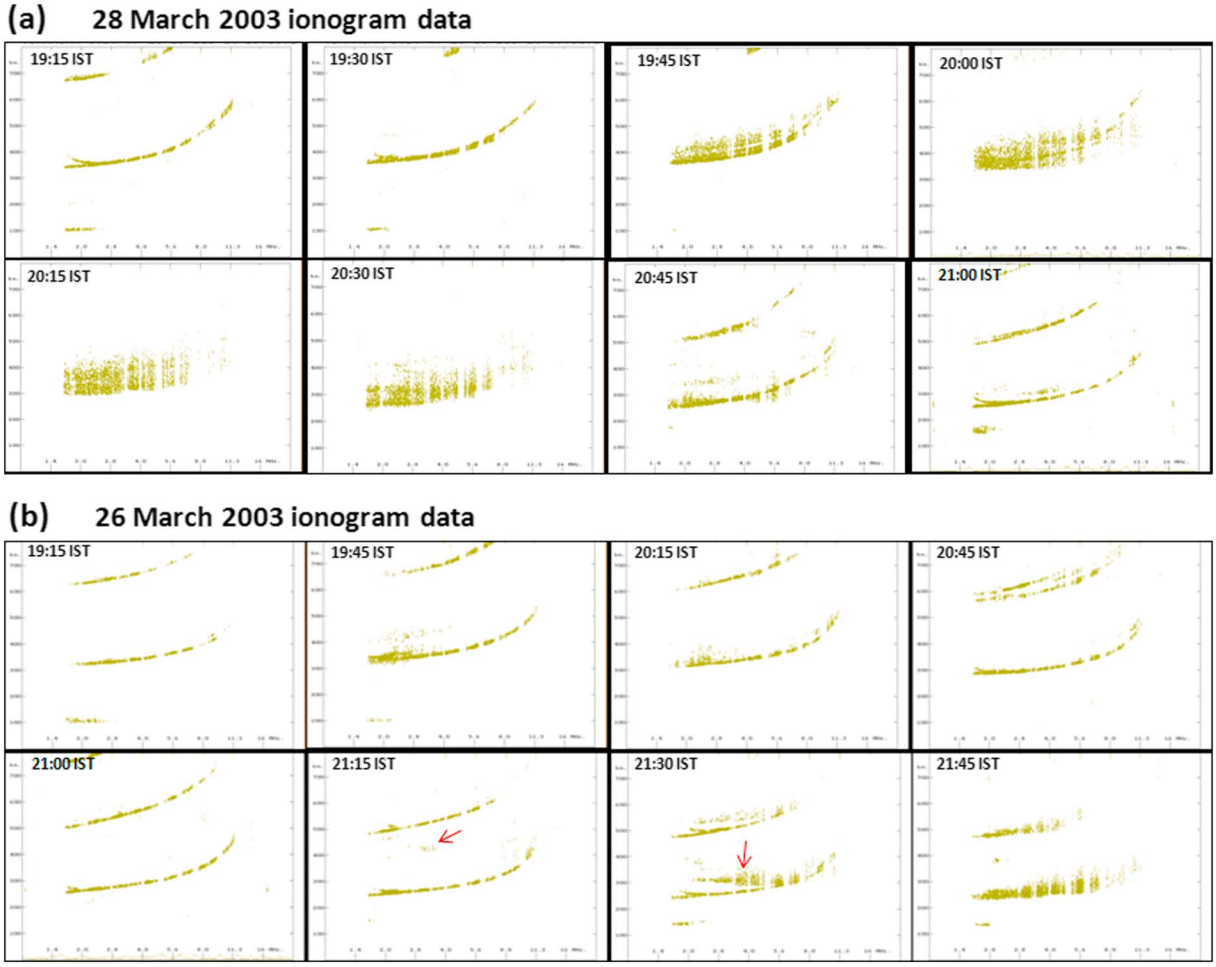

Figure 2. Ionogram data recorded on (a) 28 March 2003 and (b) 26 March 2003.

However, bottomside radar echoes were seen between 19:30 IST and 20:30 IST. Bottomside radar echoes differ from the radar plumes and remain confined to the bottom of the *F* region.

The ionogram data recorded over Sriharikota on 28 and 26 March 2003 are indicated in Figures 2a and 2b, respectively. On 28 March the range spread *F* (RSF) appeared in the ionogram at 19:45 IST and persisted for about an hour. It must be mentioned here that unlike the vertically elongated radar plumes, spread *F* happens because of the oblique arrival of the high-frequency (HF) echoes. Thus, if the irregularities are present in the *F* region over the ionosonde location, oblique echoes will cause the *F* trace to spread. Ionograms recorded on 26 March indicate bottomside spread *F* (BSSF) in the postsunset hours, with clean ionogram recorded at 20:45 IST. BSSF differs from the RSF and is identified by the spread in the bottom edge of the *F* trace. This indicates its linkage with the presence of plasma density discontinuities in the bottom of the *F* layer. RSF was seen in the ionogram recorded at 21:45 IST, close to the time radar plume that was observed by the Gadanki VHF radar (Figure 1b). An interesting aspect of the ionograms data is the echoes observed at greater range than the main *F* trace prior to the RSF. These echoes observed in the ionograms recorded at 21:15 and 21:30 IST are indicated with red arrows in Figure 2b. Range separation between these echoes and the *F* trace is lesser in the ionogram recorded at 21:30 IST than at 21:15 IST. This indicates that these echoes have come from reflectors located in the oblique direction, which finally arrived overhead at 21:45 IST to cause RSF. This provides us the clue that the EPBs on 26 March were not freshly generated over Sriharikota but drifted from a westward location. In the mid solar activity conditions the eastward drift of the ionospheric irregularities is usually in the range of 80 to 100 m/s [*Fejer et al.*, 2005]. As ionosonde has a very large beam width ($>$ 60°), it is perhaps possible to observe the *F* region irregularities

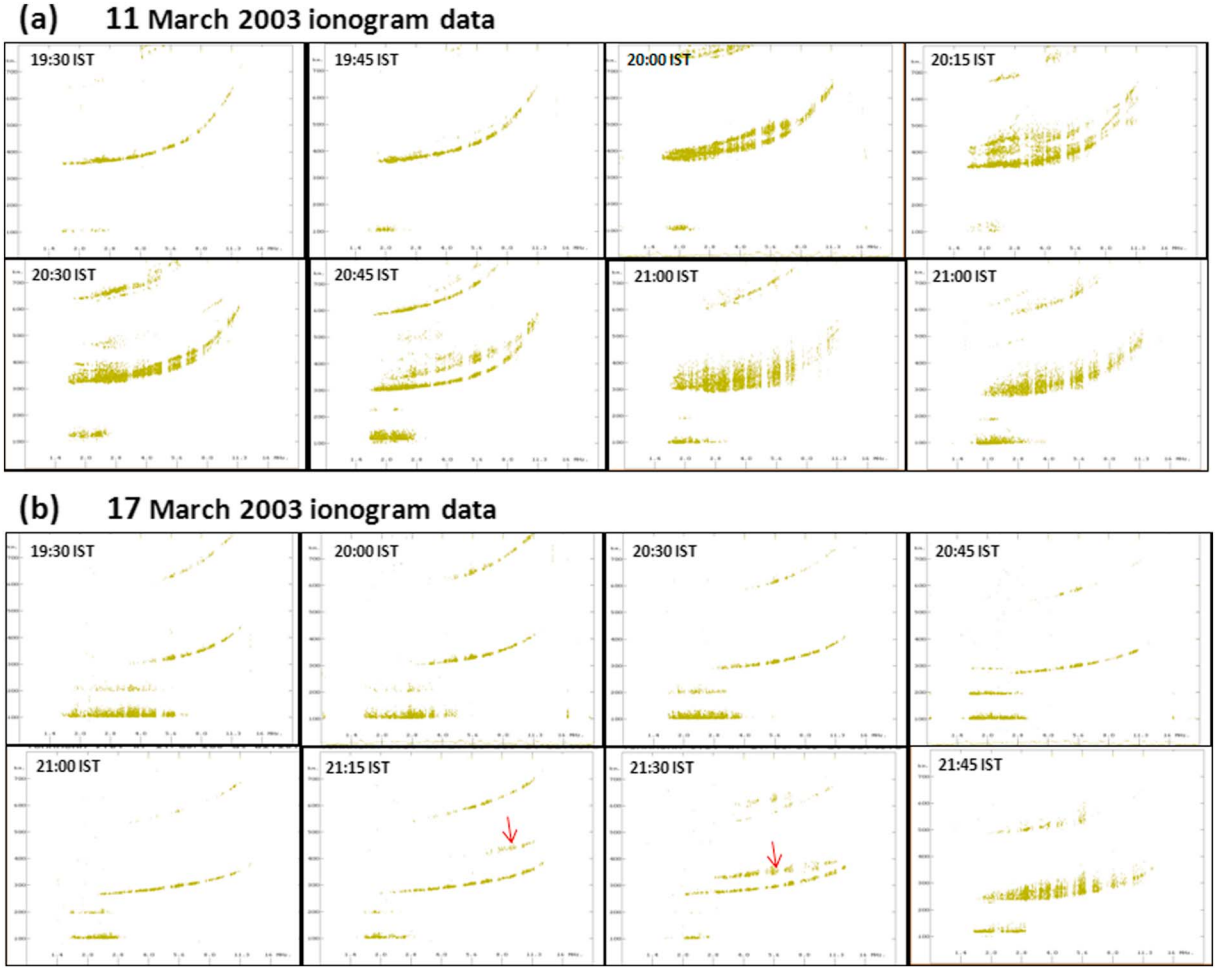

Figure 3. Ionogram data recorded on (a) 11 March 2003 and (b) 17 March 2003.

much before it arrives overhead. Recently, *Lynn et al*. [2011] have developed the ionogram range-time analysis technique to estimate the zonal eastward drift in the *F* region considering the oblique echoes. However, the exact longitude of the *F* region irregularities in case of oblique echoes cannot be defined as the ionosonde measures the virtual range (and not the real range) and also the HF waves will not travel a straight path (due to refraction). In a simple estimation, with a beam width of $>60°$, ionosonde will be able to observe the presence of irregularities at *F* region altitudes >150 km off zenith. As the coordinated VHF radar and ionosonde data are limited, a detailed case study of the two categories has been carried out utilizing the ionosonde data alone.

3.2. Detailed Cases Study Based on Sriharikota Ionosonde Data

3.2.1. Ionosonde Observation on 11 and 17 March 2003

One more example each of category 1 and category 2 spread *F* observation over Sriharikota is shown in Figure 3. Figures 3a and 3b present ionograms recorded on 11 March 2003 and 17 March 2003, respectively. On 11 March the onset of the RSF happened at 20:00 IST concurrent with the peak *h'F* time, and this case belongs to category 1 observation. Ionograms recorded on 17 March indicate delayed onset of RSF. RSF appeared in the ionogram at 21:45 IST (significantly delayed in comparison with 11 March). Prior to the onset of the RSF oblique echoes were recorded at higher range, indicated with red arrows in Figure 3b at 21:15 IST and 21:30 IST. The range separation between the main *F* trace and the oblique echo was lesser at 21:30 IST than at 21:15 IST. This indicates that the reflector (or cluster of reflectors) was drifting eastward and arrived overhead at 21:45 IST, resulting in the onset of RSF. Another important aspect seen in Figure 3b is the predominant presence of the blanketing-type sporadic *E* (E_s).

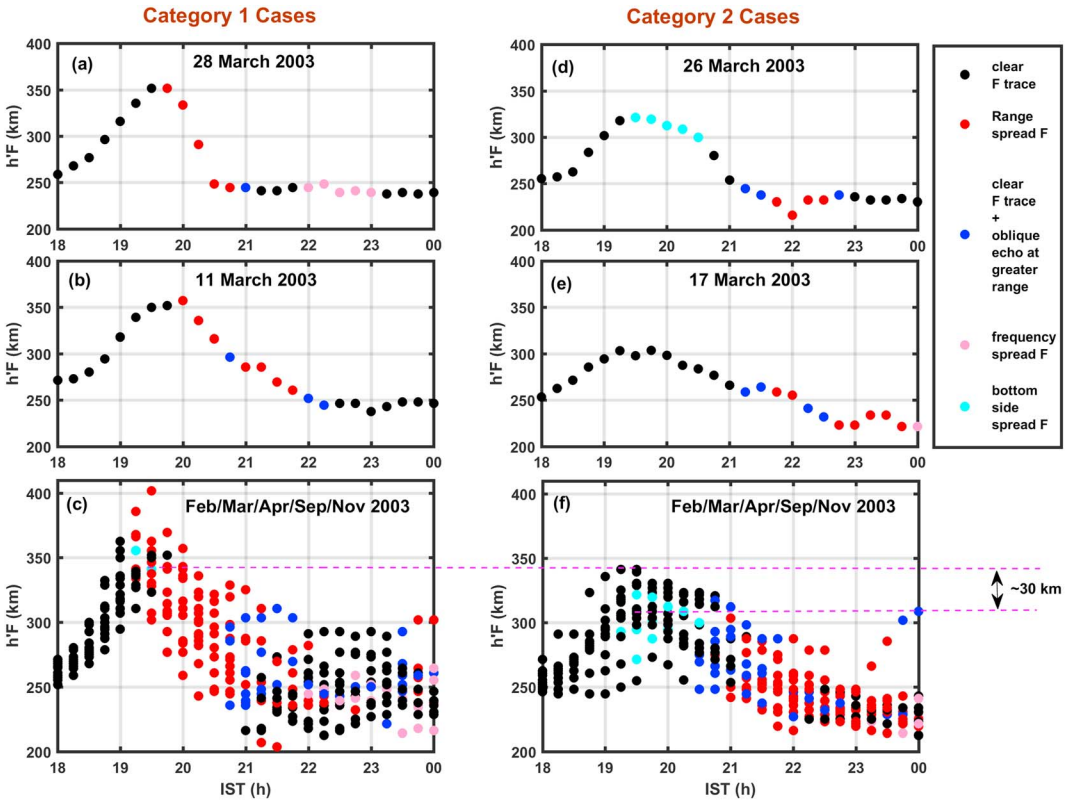

Figure 4. *h′F* corresponding to (a–c) category 1 and (d–f) category 2 cases. Color of the dots is used to indicate the nature of the ionogram.

3.2.2. *h′F* and the Nature of Ionogram Observation: Detailed Case Study

The height of the *F* layer plays the dominant role in the genesis of EPB. Due to the prereversal enhancement of zonal eastward electric field, the height of the *F* layer increases in the postsunset hours. Height variation of the *F* layer for the two categories of spread *F* observations has also been examined and is presented in Figure 4. Figures 4a–4c (Figures 4d–4f) present the *h′F* corresponding to category 1 (category 2) spread *F* observations. Figures 4a and 4b present the *h′F* over Sriharikota on 28 March 2003 and 11 March 2003, respectively. Here the color of the dot indicates the nature of the corresponding ionogram. Black, red, and pink indicate clear *F* trace, range spread *F*, and frequency spread *F*, respectively. Blue dot indicates that a clear *F* trace was seen in the ionogram along with the oblique echoes seen at a higher range. Cyan indicates the presence of bottomside spread *F*. *h′F* corresponding to the two category 2 spread *F* observations presented earlier in Figures 2b and 3b, i.e., 26 March 2003 and 17 March 2003, is shown in Figures 4d and 4e, respectively. Looking at the color of the dots, one can find that on 28 and 11 March (category 1), the onset of the RSF happened at the peak *h′F* time, whereas on 26 and 17 March the onset of RSF happened more than 1.5 h after the peak *h′F* time. Another interesting aspect is the height rise itself. The peak *h′F* was recorded more than 350 km on 28 and 11 March, while the peak *h′F* was somewhat less on 27 and 17 March.

A detailed case study has been carried out comprising all the cases in 2003 where the onset of RSF happened at or before the peak *h′F* time. A comparison of these cases has been made with all the cases where the onset of the RSF took place more than 90 min after the peak *h′F* time. Ionosonde observations during equinox months in 2003 have only been considered for this detailed case study. Figures 4c and 4f present the *h′F* corresponding to the entire category 1 and category 2 observations, respectively. Here again, the color of the dots indicates the nature of the ionogram. Important points that can be noted here are the following: (a) peak *h′F* in category 1 is significantly larger than that in category 2 and (b) the onset of the RSF in category 2 is preceded by the presence of the oblique echoes in the ionograms. RSF in category 1 can also be seen to end with the presence of oblique echoes as indicated by blue dots. Plausibly, the irregularities in this case have drifted eastward away from the field of view of the ionosonde. This implies that the *F* region

irregularities do not occur in continuation in all longitudes and its manifestation in terms of RSF in the ionograms will depend on whether the irregularities are present overhead or not. The genesis of EPBs in the category 1 has occurred in the close vicinity of the Sriharikota longitude, while the EPBs in category 2 have migrated over Sriharikota from a westward longitude. One can see that the *h'F* in the category 2 at the time of the onset of the RSF is mostly ~250 to 270 km (even though the peak *h'F* in category 2 is mostly >300 km). *h'F* ~250 to 270 km is much less than the minimum threshold height ~290 km reported earlier by *Joshi et al*. [2013b] for the genesis of the EPB to happen. This further implies that the EPBs in the category 2 have occurred in a westward longitude at an earlier local time (when *F* layer was at a higher height, plausibly peak *h'F* time) and drifted eastward to be overhead Sriharikota at the RSF onset time. This can be explained considering the presence of the large-scale wave structures. It is known that the EPBs are generated in the vicinity of the crest of the LSWS [*Tsunoda*, 1983]. In category 1 the crest of the LSWS was possibly located over Sriharikota where the genesis of the EPBs happened. On the other hand, in category 2 it was the trough of the LSWS that was located over Sriharikota, with crest located at a westward longitude where the genesis of the EPBs happened. This aspect is further corroborated by the fact that the average peak *h'F* in category 1 was ~30 km more than that in category 2. The average peak *h'F* in category 1 was ~342 km, and its standard deviation was 19.8 km, while the average peak *h'F* in category 2 was ~310 km, and its standard deviation was 19.6 km. LSWS has been known to evolve as a standing wave with insignificant zonal propagation [*Tsunoda and Ecklund*, 2007]; thus, in its presence the *F* layer height rise is expected to be more intense over the crest region than over the trough.

3.2.3. Low-Latitude E_s Observation

The height of the *F* layer and the low-latitude *E* region conductivity are the two important factors that determine the instability of the *F* layer. While higher *F* layer enhances the growth of the collisional R-T instability, conducting *E* regions can suppress the genesis of the EPB by short circuiting the *F* region polarization electric field [*Stephan et al*., 2002]. Recently, *Joshi et al*. [2013a, 2013b] have reported that the presence of the blanketing-type E_s in the low latitudes can suppress the genesis of the EPBs and plays an important role in explaining the day-to-day variability of the ESF. Also, the low-latitude *E* region conductivity has been known to influence the evening electrodynamics related with the prereversal enhancement (PRE). It thus makes sense to look at the low-latitude E_s conditions in the two different categories of spread *F* observations. Figure 5 presents the low-latitude E_s parameters observed by the Shriharikota ionosonde in the two different categories. Here Figures 5a–5d present the top frequency of the E_s (ft*Es*), blanketing frequency of E_s (fb*Es*), height of E_s (*h'E*), and occurrence (%) of blanketing E_s or *Es*b, respectively, in category 1 cases. Figures 5e–5h present the similar E_s parameters but for category 2 cases. The most visible difference in the E_s parameters in the two categories is the absence of the blanketing-type E_s during 19:30 IST to 20:30 IST in category 1 cases. Complete disappearance of fbE_s values can be seen during this period in Figure 5b. Such disappearance of fbE_s values cannot be seen in Figure 5f.

Coming to the height migration of the E_s in the two categories indicated in Figures 5c and 5g, E_s height can be seen to be ~100 km. Later in the night after ~21:00 IST, the height of the E_s can be seen descending from ~140 km. Formation and migration of descending E_s layers are known to be controlled by the semidiurnal and terdiurnal tidal forcing. Thus, the observation of the descending nature of the E_s layer highlights the important role played by the neutral wind system (tides and gravity wave winds) in its formation at low latitudes. Figures 5d and 5h, which show the occurrence (%) of the blanketing E_s in the two categories, indicate the nature of the E_s in the two categories to be different. In category 1 cases (Figure 5d) the occurrence of the *Es*b was zero during 19:30 IST to 20:30 IST period. In category 2 cases (Figure 5h) the *Es*b occurrence was more than 50% during the same period. It must be mentioned here that 19:30 IST to 20:30 IST is usually the time of the *F* layer attaining the peak height due to the PRE and also the time of the genesis of the EPB. Possibly, the occurrence of the *Es*b over Sriharikota during that period in category 2 cases resulted in the suppression of the EPB genesis over Sriharikota longitude by short circuiting the polarization electric field [*Stephan et al*., 2002; *Joshi et al*., 2013a, 2013b]. Spatial observation of low-latitude E_s could not be made with the current observational setup used for the investigation. Earlier investigations, however, have revealed large spatial variation of low-latitude E_s. *Raizada and Sinha* [2000] have found large variation in the E_s conditions in ascent and decent measurements of plasma density in a rocket experiment from Sriharikota, carried out to investigate the spread *F* irregularities. Such difference in the upleg and downleg measurement can be attributed to the spatial variation of E_s.

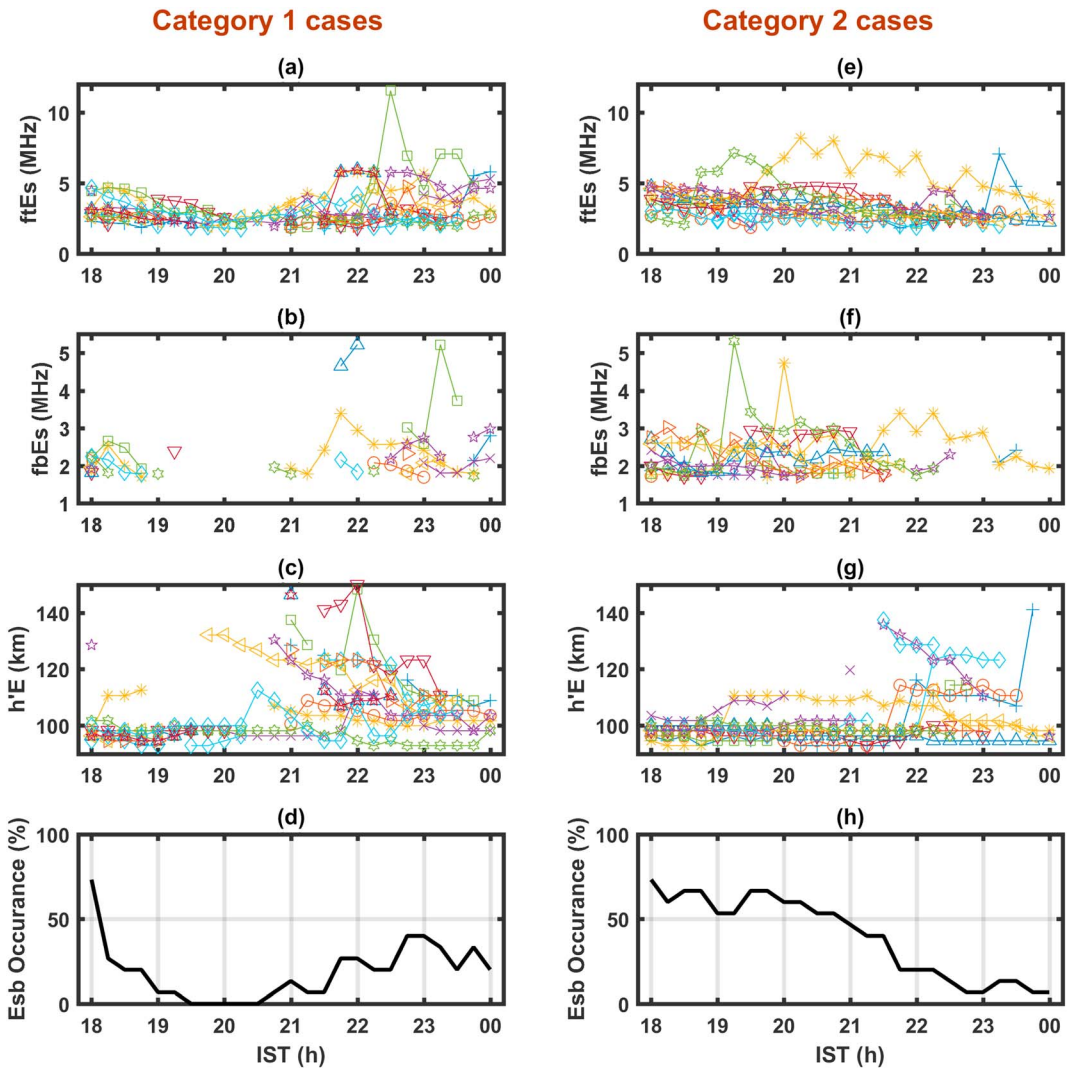

Figure 5. (a) ftE_s, (b) fbE_s, (c) $h'E$, and (d) occurrence of blanketing E_s for category 1 observations. (e) ftE_s, (f) fbE_s, (g) $h'E$, and (h) occurrence of blanketing E_s for category 2 observations.

There also exists limitation in the observation of the E_s using the ionosonde. The range resolution of the ionosonde is ~3 km which is insufficient to characterize the height profile of E_s layers. Also, the scattering/reflection from plasma irregularities at off vertical angles will mix with the vertically reflected signals, making it difficult to derive E_s profile (E_s just appears as a slab in the ionograms). As the reflection occurs from the bottomside, ionosonde cannot provide measurements of the topside profile of the E_s. Thus, the useful E_s parameters observed with an ionosonde are ftE_s, fbE_s, and $h'E$. E_s has been characterized based on these parameters only. *Joshi et al.* [2013a, 2013b], based on a detailed investigation on the linkage between the low-latitude E_s and the genesis of the EPB, hypothesized the blanketing frequency of the E_s to be a better indicator (than the top frequency of E_s) of the presence of conducting E_s layer capable of short circuiting the F region electric filed. As far as the top frequency of the E_s (ftE_s) is concerned, it represents the peak plasma density of the plasma patches located anywhere in the ionosonde's field of view, which are capable of reflecting/scattering the radio waves. However, the blanketing frequency (fbE_s) indicates the background peak plasma density of the E_s layer. Radio wave frequencies below blanketing frequency will not be able to penetrate up in the ionosphere. As far as the conductivity of the E_s layer is concerned, it is considered to depend on the background plasma density of the E_s layer rather than on the peak plasma density of the plasma patches. Modeling investigation on the generation of LSWS linked with the spatial undulation of low-latitude E_s is presented next.

3.3. Model Computation of the Longitudinal Undulation in the *F* Layer Height Rise

Vertical electric field in the equatorial *F* region during the postsunset period is controlled by the neutral wind-driven *F* region dynamo. Simplified expression for the vertical electric field can be written as [*Kelley*, 2009]

$$E_Z = -UB\frac{\Sigma P^F}{\Sigma P^F + \Sigma P^E} \tag{1}$$

where E_Z is the vertical *F* region electric field over equator, *U* is the zonal thermospheric wind, *B* is the Earth's magnetic field, and $\frac{\Sigma P^F}{\Sigma P^F + \Sigma P^E}$ is the ratio of the *F* region field line integrated Pedersen conductivity to total field line integrated Pedersen conductivity (i.e., *F* region + *E* region). During the daytime *E* region field line integrated Pedersen conductivity is quite large in comparison to the *F* region, so the vertical field during the daytime originates in the *E* region. As the Sun sets and the production of photoionization in the *E* region ceases, *E* region field line integrated Pedersen conductivity decreases. Now the large eastward zonal wind in the *F* region becomes the primary driver of the vertical *F* region field as in equation (1).

During the evening hours, there exists a westward gradient in the conductivity in the low-latitude *E* region. Hence, there exists a zonal divergence in the hall current in the low-latitude *E* region, being produced by the field line mapping of the *F* region vertical field. The divergence of the current will produce the charge pileup given by equation (2)

$$\nabla . J_H = -\frac{\partial q}{\partial t} \tag{2}$$

where J_H is the hall current density and *q* is the charge. The negative sign in the equation signifies that the charge pileup will produce electric field to oppose the divergence in the source current. Under steady state the divergence will be zero. Thus, the amount of divergence in the hall current will decide the magnitude of the electric field generated. The current density is related to the electric field as (Ohm's law)

$$J = \sigma E \tag{3}$$

Thus, under steady state equation (2) can be written as

$$\nabla J_H = -\nabla(\sigma_P E) \tag{4}$$

where σ_P is the Pedersen conductivity. This can be understood as under steady state, Pedersen current will flow in the *E* region (driven also by the electric field generated by the charge pileup due to the divergence of the Hall current) to make the overall current divergence free. For such Pedersen current to flow, enhanced electric field must set in. Considering only the current density and Pedersen conductivity variation in zonal direction, we get

$$\frac{\partial J_{Hx}}{\partial x} = -\sigma_P \frac{\partial E_x}{\partial x} - E_x \frac{\partial \sigma_P}{\partial x} \tag{5}$$

Simplifying for ∂E_x, we get

$$\partial E_x = -\frac{\partial J_{Hx}}{\sigma_P} - E_x \frac{\partial \sigma_P}{\sigma_P} \tag{6}$$

Here ∂E_x is the additional zonal electric field generated in the *E* region to make the current divergence free, and E_x is the existing zonal electric field. It can be understood from equation (6) that if the conductivity gradient (Hall as well as Pedersen conductivity) is westward (eastward), ∂E_x will be positive (negative). This generated electric field can map along the field line to the *F* region and add up to the zonal field. *Farley et al.* [1986] considered the divergence of the hall current in the low-latitude *E* region as the main reason behind the prereversal enhancement (PRE) of zonal electric field and the postsunset height rise of the *F* layer. Gradient in the hall conductivity, however, need not be uniform due to the presence of the E_s. If that is the case, the postsunset height rise will show longitudinal variation. This aspect has been investigated using the model computation.

3.3.1. Electron Densities in the *E* Region During the Evening Hours

Figure 6a shows the electron densities in the low-latitude *E* region based on IRI model, in the postsunset period. At the reference point (0 km distance) the local time is 1800 h, while 2000 km east of it has a local time of 1912 h. This is due to the fact that sunset traverses from east to west and covers 2000 km in about 1 h and 12 min. One can notice a westward electron density gradient that exists during the evening hours. IRI model,

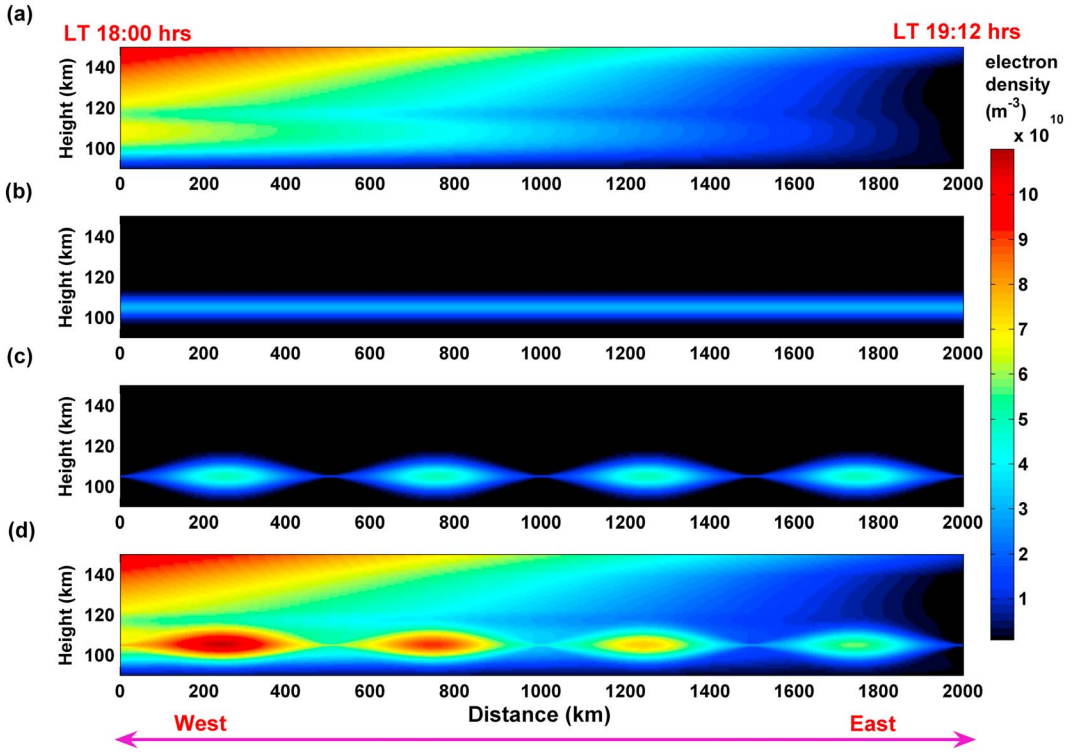

Figure 6. Low-latitude *E* region considered in the model computation. (a) *E* region based on IRI model. (b) Hypothetical nighttime E_s layer slab. (c) Large-scale E_s patches generated by redistributing the E_s slab of Figure 6b. (d) Aggregate of the ionization shown in Figures 6a and 6c. For details, refer to the text.

however, does not include the E_s characteristics. The postsunset time peak electron densities owing to the metallic ion layers (nighttime E_s) observed using the ionosonde were found to be much larger than the one based on the IRI model. Various reports have indicated the presence of variable metallic ion layers with large plasma densities during the postsunset periods [e.g., *Earle et al*., 2000]. For the investigation requirement, hypothetical metallic ion layer as shown in Figure 6b has also been assumed to exist in the *E* region. Here the metallic ion layer is assumed to be uniform across the 2000 km east-west stretch. This, however, may not be the case always due to the action of the gravity wave-induced convergence. Therefore, in the model, metallic ion layer has been redistributed in the form of 500 km scale hypothetical E_s patches as shown in Figure 6c. Metallic ion layer has been redistributed in such a way that total metallic ion content in Figures 6b and 6c remains the same. Basically, the metallic ion layer-related ionization has been redistributed. Also, the E_s patches have been assumed to be stationary with negligible zonal propagation. Figure 6d shows the combined *E* region electron densities that will exist if the electron densities in Figures 6a and 6c are added up. Figure 6d is basically the aggregate of Figures 6a and 6c. The peak electron density of E_s presented in Figure 6c is $\sim 5 \times 10^{10}\,\mathrm{m}^{-3}$, which corresponds to a plasma frequency of ~2 MHz. One can note that the E_s blanketing frequency in Figure 5 is also mostly 2–2.5 MHz. Thus, the electron densities of the E_s considered in the model are in accordance with the observations. It must be mentioned here that the formation of patchy/nonpatchy E_s at nonequatorial latitudes is controlled by transport and convergence of plasma due to the action of tidal and gravity wave winds [*Mathews and Bekeny*, 1979; *Carter and Forbes*, 1999]. Several investigations have revealed the presence of metallic ion layers during the nighttime having significant peak plasma density (even comparable to that in the daytime) [e.g., *Earle et al*., 2000; *Bishop and Earle*, 2003; *Roddy et al*., 2007]. Variability of metallic ion layers has been found to depend on the tidal and gravity wave wind variability. The *E* region presented in Figure 6 has been subjected to the *F* region wind-driven vertical electric field in the model computation to investigate the postsunset height rise of the *F* layer.

3.3.2. Computing the *F* Layer Height Rise

For the model computations presented in this paper, the plasma densities in the *E* and *F* regions have been considered in accordance with the IRI model. NRLMSISE00 model [*Picone et al*., 2002] has been used to derive

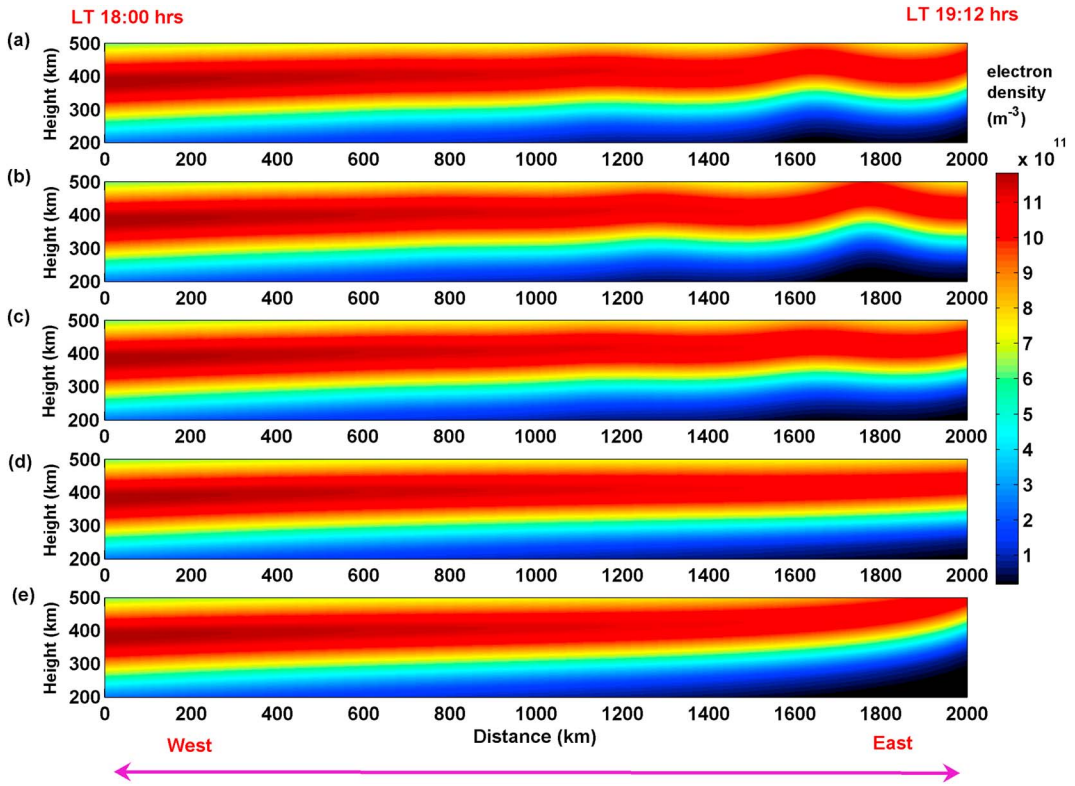

Figure 7. Height migration of the *F* layer in the model computation for five different *E* region scenarios. For details, refer to the text.

the thermospheric density profile. Thermospheric density profile has been used to derive the ion-neutral collision frequency. Pedersen conductivity has been calculated using the plasma density and collision frequency. Eastward neutral wind of 200 m s^{-1} has been assumed to exist in the *F* region. *Farley et al.* [1986] have also assumed the eastward thermospheric neutral wind to be 200 m/s in their simulation of *F* layer height rise. The zeroth-order *F* region zonal electric field, due to the charge pileup at dusk terminator, has been assumed to be 0.4 mV/m (eastward) at 18:00 IST, which reduced gradually to −1 mV/m (westward) at 19:12 IST. Hence, the electric field due to the background charge pileup at dusk sector has been assumed to be predominantly westward oriented, while the electric field produced due to the divergence of the hall current in the conjugate *E* regions has an eastward value. The sum of the two provides the total electric field which comes out to be eastward.

Figure 7a shows the height migration of the *F* layer over magnetic equator brought out by the model computation, assuming the conjugate low-latitude *E* region to be similar to the one shown in Figure 6d. Here the *F* region initial profile at 18:00 IST at the reference location (0 km) has been taken from the IRI model. Subsequently, with time the peak plasma density and the density gradients above and below the peak have been varied, also in accordance with the IRI model. This has been done in order to account for the loss of ionization due to the recombination process, which results in the reduction of the *F* region field line integrated Pedersen conductivity. The height migration of the *F* layer has been calculated based on the eastward electric field being generated due to the divergence of hall current in the low-latitude *E* regions. Figure 7a clearly shows the large-scale zonal undulation in the height of the *F* layer. Figure 7b shows the height migration of the *F* layer, when the phase of the E_s patch in the low-latitude *E* region has been varied by 180°. In other words, the location of the plasma density troughs and crests of Figure 6c has been interchanged. It must be mentioned here that the low-latitude E_s patch has been assumed to be stationary with negligible propagation. Hence, the model has produced the standing undulations in the *F* layer height.

So far, the conjugate *E* regions have been assumed to be similar, which may not be the case always. Therefore, in the model computation, the conjugate *E* regions have been made dissimilar. While the *E* region

in one hemisphere has been assumed to be represented as shown in Figure 6d, in the other hemisphere the *E* region is assumed to be the aggregate of Figures 6a and 6b. This means that in one hemisphere the E_s has been assumed to be in the form of spatially uniform slab as shown in Figure 6b, while in the other hemisphere the E_s has been assumed to be in the form of large patches. In other words, the field line integrated Pedersen conductivity of the *E* region owing to the E_s in one hemisphere has a zonal uniform moderate value, while in the other hemisphere, it varies in a sinusoidal fashion from very low to quite high. The effect of such an asymmetry in the conjugate *E* regions, on the height migration of the *F* layer, is shown in Figure 7c. It shows a similar spatial undulation as in Figure 7a, but with reduced amplitude.

It is also important to see the effect on the height rise pattern of the *F* region when conjugate *E* regions are symmetric with spatially uniform E_s, i.e., the aggregate of Figures 6a and 6b. Such an example is presented in Figure 7d. One can note that there is no spatial undulation in the *F* layer height in this case. Also, the height rise of the *F* layer is quite less than in the case of Figure 7a. This is also due to the fact that the enhanced field line integrated Pedersen conductivity of the *E* region reduces the magnitude of the *F* region vertical field, given by equation (1). This in turn reduces the magnitude of the hall current in the low-latitude *E* region and hence its divergence also. This aspect has been investigated previously by *Fesen et al*. [2000]. *Fesen et al*. [2000] based on TIEGCM model investigations have found that the *E* region plasma density $>$3300–7500 el/cm^3 ceases the PRE development by short circuiting the *F* region dynamo.

Although the formation of E_s in the low latitudes during the postsunset period is a common phenomenon, its occurrence on every evening, however, is not guaranteed [*Joshi et al*., 2013a, 2013b]. Thus, it is important to assess the postsunset height rise in the absence of any type of E_s whatsoever. Figure 7e presents the height migration of the *F* layer in the model simulation, when low-latitude *E* regions were represented by Figure 6a (no E_s whatsoever). It is interesting to find that the height rise of *F* layer is highly intense, as compared to other scenarios discussed in Figures 7a–7d. Also, the large-scale undulation in the *F* layer height is absent.

3.4. Implication on the R-T Instability

Growth rate of the R-T instability varies exponentially with the height of the *F* layer. This is because the ion-neutral collision frequency decreases exponentially with height and the fact is that the growth rate of the R-T instability is proportional to g/ν_{in} where g is the acceleration due to gravity and ν_{in} is ion-neutral collision frequency. This being true, the effectiveness of the g/ν_{in} depends also on the ratio of the *E* and *F* region field line integrated Pedersen conductivity [*Stephan et al*., 2002]. *Joshi et al*. [2013a] termed the ratio of *F* region field line integrated Pedersen conductivity to the total field line integrated Pedersen conductivity as growth efficiency, which theoretically varies between 0 and 1. In order to understand the impact of the large-scale zonal undulations of the *F* layer height on the growth rate of the R-T instability, both growth efficiency and g/ν_{in} have to be investigated for five different scenarios presented in Figure 7.

Green, red, blue, and purple curves in Figure 8a show the growth efficiencies $\left(\frac{\Sigma P^F}{\Sigma P^F+\Sigma P^E}\right)$ as a function of magnetic field apex height over the equatorial *F* region at 19:12 IST, i.e., at 2000 km from the reference location (0 km), corresponding to the scenarios presented in Figures 7a–7d, respectively. In Figure 8b, the black curve shows the g/ν_{in} as a function of height, and green, red, blue, and purple stars indicate the *F* layer base height at 19:12 IST, corresponding to the scenarios presented in Figures 7a–7d, respectively. The black circle in Figure 8b indicates the *F* layer base height for the scenario presented in Figure 7e, whereas the growth efficiency for the scenario presented in Figure 7e will be quite close to unity, i.e., 100% (due to the absence of E_s in the low latitudes). Thus, the scenario presented in the Figure 7e has the highest value of g/ν_{in} as well as the highest growth efficiency. Among the scenarios, where low-latitude E_s was present, the one presented in Figure 7a has the highest value of growth efficiency and g/ν_{in}, as indicated in Figure 8 (green). The scenario presented in Figure 7b is similar to that in Figure 7a, except for the fact that the locations of *F* layer height crests and troughs are interchanged. Therefore, the red curve in Figure 8a and the red star in Figure 8b indicate the growth efficiency and g/ν_{in} at the trough region of the large-scale wave structure. It can be noted that the trough region has the minimum value in Figures 8a and 8b (red). Blue curve in Figure 8a and blue star in Figure 8b indicate the growth efficiency and g/ν_{in}, respectively, corresponding to the scenario where one hemisphere has spatially uniform E_s slab while other has large-scale E_s patches. These values are smaller than those shown in green. Purple curve in Figure 8a and purple star in Figure 8b indicate the growth

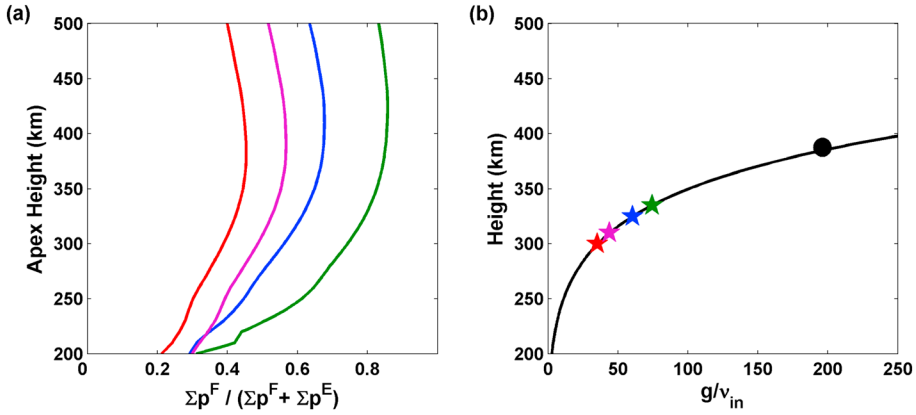

Figure 8. (a) Green, red, blue, and purple curves represent $\frac{\Sigma P^F}{\Sigma P^F + \Sigma P^E}$ at the magnetic field apex over magnetic equator at 19:12 LT for the *F* region model output presented in Figures 7a–7d, respectively. (b) Black curve indicates the g/ν_{in} value as a function of height during the high solar activity period. Here green, red, blue, and purple stars indicate the height of the *F* layer at 19:12 LT for the *F* region model output presented in Figures 7a–7d, respectively. The height of the *F* layer at 19:12 LT for the *F* region model output presented in Figure 7e is indicated by black circle.

efficiency and g/ν_{in}, respectively, corresponding to the scenario where both the hemispheres are assumed to have spatially uniform E_s slab. These values are significantly smaller than those corresponding to the cases with large-scale wave structures (i.e., green and blue curves).

Therefore, if the large-scale zonal undulation in the height of the *F* layer is being generated by E_s in the low latitude, it will influence the R-T instability by modifying both the growth efficiency and g/ν_{in}. However, the growth of the R-T instability (in terms of growth efficiency and g/ν_{in}) will be highest when the E_s in the low latitudes are absent.

4. Discussion and Concluding Remarks

Two categories of spread *F* observations are discussed in this paper, category 1 where the onset of the RSF was concurrent with the peak *h'F* and category 2 where the onset of the RSF happened more than 90 min after the peak *h'F* time. While the genesis of the EPB is likely to happen at or before the peak *h'F* time, its manifestation in terms of the RSF will depend on whether the EPB is located overhead or not. RSF in the category 2 cases was preceded by the appearance of oblique echoes in the ionograms, whose range decreased with time till it merged in the RSF. This indicates the eastward drift of the reflectors. This implies that EPBs in category 2 were not freshly generated over Sriharikota. Also, the *h'F* at the time of the onset of RSF in category 2 cases was mostly in the range of 250–270 km, which is quiet less than the threshold height for the EPB genesis reported earlier [*Joshi et al.*, 2013b]. Thus, it has been argued that the genesis of the EPBs in category 2 cases also happened at peak *h'F* time over a western longitude and drifted eastward to be detected by the ionosonde at RSF onset time. *Yokoyama et al.* [2004] based on comprehensive scanning EAR radar observation have also reported the EPB genesis time to be close to *F* region sunset (~19:30 LT). Interestingly, the peak *h'F* in category 1 cases on average was ~30 km higher than that in the category 2 cases. This plausibly indicates the presence of LSWS. Day-to-day variability of the *F* layer height rise is expected to show its influence in the two categories alike. The standard deviations of the peak *h'F* in the two categories were nearly the same ~19.5 km. However, the difference in the average peak *h'F* in the two categories was ~30 km. Nearly similar standard deviation indicates that the intrinsic variability of PRE (day-to-day variability) in each category was alike. However, the difference in the mean peak *h'F* in the two categories was much higher than the standard deviation. This indicates that another factor (LSWS) was responsible for the difference in the mean peak *h'F* in the two categories. This further indicates that the height difference in the two categories was not linked with the day-to-day variability of the PRE. Characteristics of the low-latitude E_s were found to be significantly different in the two categories at peak *h'F* time (19:30 to 20:30 IST). Thus, it has been argued that the spatial modulation of low-latitude E_s can be a cause of the formation of LSWS through *E-F* region coupling process.

Model computation also highlights the role of the low-latitude E_s on the zonal pattern of the postsunset height rise of the *F* layer. When the E_s during the postsunset period was considered to be spatially uniform and symmetrical at the conjugate low latitudes, it resulted in a spatially uniform, time-dependent postsunset height rise in model computation. However, when the same ionization was redistributed in the form of zonal patches of E_s, the result was in the form of spatial undulations in the *F* layer height. The amplitude of this undulation depends on the overall zonal gradient of the low-latitude E_s conductivity. When the low-latitude E_s in conjugate hemispheres was assumed to be asymmetric, the undulation in the *F* region height had smaller amplitude. Also, when the E_s in the low latitudes were assumed to be absent, the height migration of the *F* layer was remarkably intense.

In order to examine the role of the large-scale zonal undulation of the *F* layer height, on the growth rate of the R-T instability, g/ν_{in} as well as the growth efficiency was evaluated. Owing to the low-latitude E_s being the subject of the discussion, the resulting large-scale undulation would influence the R-T instability by changing the g/ν_{in} and also by modifying the growth efficiencies. The scenario in which low-latitude E_s in the conjugate hemispheres has been considered to be symmetrical in the form of large-scale patches, resulting large-scale undulation of the *F* layer height in the model computation, has highest (lowest) values of both g/ν_{in} and growth efficiency at the crest (trough) region, among the four different scenarios where E_s were assumed to be present in the low latitudes. Thus, merely the height rise associated with the large-scale undulation of *F* layer height alone must not decide its impact on the R-T instability. Although the growth of the R-T instability on a given night will depend greatly on the amplitude of the seed perturbation, assuming the amplitude of the initial seed perturbation to be constant, case with no E_s in the low latitudes will have the highest growth. This will be followed by the case where the E_s in the low latitudes is in the form of large-scale patches and *F* layer displays large-scale height undulations, while the case with spatially uniform E_s and no large-scale undulation in the *F* layer height will have the least growth of the R-T instability. Thus, the mere presence of the large-scale undulation in the *F* layer height must not dictate the formation of the ESF. In the absence of low-latitude E_s and with large postsunset height rise of the *F* layer, ESF can occur in the absence of large-scale height undulation.

Earlier investigations on *E-F* region coupling processes pertaining to the evening ionosphere have considered a different cause-effect sequence [*Abdu et al*., 2003; *Carrasco et al*., 2007; *Batista et al*., 2008]. *Abdu et al*. [2003] have considered the sheared vertical PRE electric field mapping along the magnetic field lines to low-latitude *E* regions as the cause of the E_s disruption. Few other investigations have reported a different aspect of *E-F* region coupling processes [*Patra et al*., 2004, 2005; *Patra*, 2008; *Li et al*., 2011]. *Patra et al*. [2004] first reported that the electric field associated with the EPB in the growth phase can map along the magnetic field line to low-latitude *E* region and cause the disappearance of low-latitude *E* region irregularities by stabilizing the *E* region plasma. Observational results reported in this investigation somewhat differ from that reported by *Abdu et al*. [2003]. First, a clear disruption of the ftE_s values at peak *h'F* time (19:30 IST) is not seen in Figure 5a. *Abdu et al*. [2003] have reported a complete disruption of ftE_s coinciding with the peak *h'F* time. Second, a sharp decline in the occurrence of the *Es*b can be seen much before the peak *h'F* time (between 18:00 IST and 19:00 IST) in Figure 5d. This indicates that the low-latitude *Es*b disruption was not caused by the vertical PRE electric field; rather, the disappearance of *Es*b caused intense *F* layer height rise. Figure 5d also indicates a reappearance of *Es*b at ~23:00 IST. If the formation/disappearance of the *Es*b is considered to be controlled by the gravity wave wind, *Es*b disappearance (formation) will occur at the wind node (antinode). Gradual resurgence of the *Es*b at ~23:00 IST possibly indicates that the antinode of the GW winds in the *E* region has propagated over the observational site, i.e., Sriharikota. Likewise, the higher occurrence of *Es*b at peak *h'F* time and its gradual decrease by 23:00 IST in Figure 5h possibly indicate that the GW winds in the second category were out of phase in comparison with that in the first category.

In general, there exist two schools of thoughts on PRE-E_s relationship. One considers the low-latitude *E* region conductivity [*Farley et al*., 1986; *Fesen et al*., 2000; *Stephan et al*., 2002; *Joshi et al*., 2013a, 2013b], particularly E_s conductivity [*Joshi et al*., 2013a, 2013b, 2012], to determine the magnitude of PRE. The other considers the ion Pedersen vertical drift in the low-latitude *E* region caused by the PRE electric field mapping as the cause of the changes in the low-latitude E_s structure. However, the issue that remains unexplained in the second is the absence of the polarization electric field that would oppose the vertical ion Pedersen drift which causes the E_s structure to change. In order to further address the cause-effect relationship, spatial measurement of

low-latitude E_s will be required. If a significant spatial difference (of appropriate scale size) in the low-latitude E_s is observed much before the peak PRE time, it will indicate that the E_s layer patches (which generates LSWS) are not created by PRE electric field mapping. However, observational setup for appropriate spatial measurement of low-latitude E_s does not exists, particularly in the Indian sector.

Earlier investigations have regarded the spatially varying dynamo current due to neutral wind perturbations in the *F* region, associated with the atmospheric gravity waves (AGWs), as the cause of the generation of LSWS [*Tsunoda et al*., 2011; *Tulasi Ram et al*., 2012, 2014]. In those investigations, it was the vertical neutral wind associated with the AGW that was considered the driver of the zonal undulation in the *F* layer height, whereas the simulation results presented in this paper indicate that the LSWS could be generated by the spatially varying *F* region dynamo linked with the spatial variation of the low-latitude *E* region conductivity, through *E-F* coupling. Such spatial variation in the *E* region conductivity could be generated by the action of AGW through the formation of E_s. In the previous case, the role of LSWS is primarily in the form of the growth rate of the collisional R-T instability, besides other factors like wind-driven cross field instability [*Tsunoda*, 1983]. Also, the presence of LSWS has been regarded as the earliest manifestation of the presence of the seed perturbation. However, if the source of the LSWS is in the *E* region conductivity, its role in the R-T instability will also be in the form of the growth efficiency $\left(\frac{\Sigma P^F}{\Sigma P^F+\Sigma P^E}\right)$. Thus, the magnitude of the large-scale zonal modulation of the *F* layer height and its effectiveness toward the onset of the R-T instability would depend also on the magnitude of zonal modulation in the *E* region conductivity in conjugate low latitudes. In this investigation the features of the blanketing E_s in the ionosonde observations have been found to be remarkably different in the two different categories of spread *F* events. The occurrence of *Es*b during 19:30 to 20:30 IST was 0% (>50%) in category 1 (category 2) cases. Although the computational results presented in this paper indicate that the spatial variation of low-latitude E_s densities can generate the large-scale spatial undulation in the *F* layer height through *E-F* region coupling process, other mechanisms proposed for the generation of the LSWS in previous investigations are not being completely ruled out.

Acknowledgments
The author is thankful to Indian Institute of Geomagnetism for the award of Nanabhoy Moos Research Fellowship (postdoctoral fellowship). The author would like to acknowledge A.K. Patra for making the radar and ionosonde data available and also for his discussions on plasma instabilities. VHF radar and ionosonde data can be obtained by contacting A.K. Patra (akpatra@narl.gov.in). The author is also thankful to the reviewer of this paper for valuable comments.

References

Abdu, M. A., J. W. MacDougall, I. S. Batista, J. H. A. Sobral, and P. T. Jayachandran (2003), Equatorial evening prereversal electric field enhancement and sporadic *E* layer disruption: A manifestation of *E* and *F* region coupling, *J. Geophys. Res.*, *108*(A6), 1254, doi:10.1029/2002JA009285.

Batista, I. S., M. A. Abdu, A. J. Carrasco, B. W. Reinisch, E. R. de Paula, N. J. Schuch, and F. Bertoni (2008), Equatorial spread F and sporadic E-layer connections during the Brazilian Conjugate Point Equatorial Experiment (COPEX), *J. Atmos. Sol. Terr. Phys.*, *70*, 1133–1143, doi:10.1016/j.jastp.2008.01.007.

Bishop, R. L., and G. D. Earle (2003), Metallic ion transport associated with midlatitude intermediate layer development, *J. Geophys. Res.*, *108*(A1), 1019, doi:10.1029/2002JA009411.

Carrasco, A. J., I. S. Batista, and M. A. Abdu (2007), Simulation of the sporadic *E* layer response to prereversal associated evening vertical electric field enhancement near dip equator, *J. Geophys. Res.*, *112*, A06324, doi:10.1029/2006JA012143.

Carter, L. N., and J. M. Forbes (1999), Global transport and localized layering of metallic ions in the upper atmosphere, *Ann. Geophys.*, *17*, 190–209, doi:10.1007/s00585-999-0190-6.

Earle, G. D., R. L. Bishop, S. C. Collins, S. A. González, and M. P. Sulzer (2000), Descending layer variability over Arecibo, *J. Geophys. Res.*, *105*, 24,951–24,961, doi:10.1029/2000JA000029.

Farley, D. T., E. Bonelli, B. G. Fejer, and M. F. Larsen (1986), The prereversal enhancement of the zonal electric field in the equatorial ionosphere, *J. Geophys. Res.*, *91*, 13,723–13,728, doi:10.1029/JA091iA12p13723.

Fejer, B. G., J. de Souza, A. S. Santos, and A. E. Costa Pereira (2005), Climatology of *F* region zonal plasma drifts over Jicamarca, *J. Geophys. Res.*, *110*, A12310, doi:10.1029/2005JA011324.

Fesen, C. G., G. Crowley, R. G. Roble, A. D. Richmond, and B. G. Fejer (2000), Simulation of the pre-reversal enhancement in the low latitude vertical ion drifts, *Geophys. Res. Lett.*, *27*, 1851–1854, doi:10.1029/2000GL000061.

Huang, C.-S., O. de La Beaujardière, P. A. Roddy, D. E. Hunton, J. O. Ballenthin, M. R. Hairston, and R. F. Pfaff (2013), Large-scale quasiperiodic plasma bubbles: C/NOFS observations and causal mechanism, *J. Geophys. Res. Space Physics*, *118*, 3602–3612, doi:10.1002/jgra.50338.

Hysell, D. L., and J. D. Burcham (1998), JULIA radar studies of equatorial spread *F*, *J. Geophys. Res.*, *103*, 29,155–29,167, doi:10.1029/98JA02655.

Hysell, D. L., M. C. Kelley, W. E. Swartz, and R. F. Woodman (1990), Seeding and layering of equatorial spread *F* by gravity waves, *J. Geophys. Res.*, *95*, 17,253–17,260, doi:10.1029/JA095iA10p17253.

Hysell, D. L., J. Chun, and J. L. Chau (2004), Bottom-type scattering layers and equatorial spread *F*, *Ann. Geophys.*, *22*, 4061–4069, doi:10.5194/angeo-22-4061-2004.

Joshi, L. M., A. K. Patra, and S. V. B. Rao (2012), Equatorial F-region irregularities during low and high solar activity conditions, *Indian J. Radio Space Phys.*, *41*, 208–219.

Joshi, L. M., A. K. Patra, T. K. Pant, and S. V. B. Rao (2013a), On the nature of low-latitude E_s influencing the genesis of equatorial plasma bubble, *J. Geophys. Res. Space Physics*, *118*, 524–532, doi:10.1029/2012JA018122.

Joshi, L. M., A. K. Patra, and S. V. B. Rao (2013b), Low-latitude E_s capable of controlling the onset of equatorial spread *F*, *J. Geophys. Res. Space Physics*, *118*, 1170–1179, doi:10.1002/jgra.50189.

Joshi, L. M., S. Balwada, T. K. Pant, and S. G. Sumod (2015), Investigation on *F* layer height rise and equatorial spread *F* onset time: Signature of standing large-scale wave, *Space Weather*, *13*, 211–219, doi:10.1002/2014SW001129.

Kelley, M. C. (2009), *The Earth's Ionosphere*, 2nd ed., Academic Press, Oxford, U. K.
Kelley, M. C., M. F. Larsen, C. LaHoz, and J. P. McClure (1981), Gravity wave initiation of equatorial spread F: A case study, *J. Geophys. Res.*, *86*, 9087–9100, doi:10.1029/JA086iA11p09087.
Li, G., B. Ning, A. K. Patra, W. Wan, and L. Hu (2011), Investigation of low-latitude *E* and valley region irregularities: Their relationship to equatorial plasma bubble bifurcation, *J. Geophys. Res.*, *116*, A11319, doi:10.1029/2011JA016895.
Li, G., B. Ning, M. A. Abdu, W. Wan, and L. Hu (2012), Precursor signatures and evolution of post-sunset equatorial spread-F observed over Sanya, *J. Geophys. Res.*, *117*, A08321, doi:10.1029/2012JA017820.
Li, G., B. Ning, M. A. Abdu, Y. Otsuka, T. Yokoyama, M. Yamamoto, and L. Liu (2013), Longitudinal characteristics of spread *F* backscatter plumes observed with the EAR and Sanya VHF radar in Southeast Asia, *J. Geophys. Res. Space Physics*, *118*, 6544–6557, doi:10.1002/jgra.50581.
Li, G., Y. Otsuka, B. Ning, M. A. Abdu, M. Yamamoto, W. Wan, L. Liu, and P. Abadi (2016), Enhanced ionospheric plasma bubble generation in more active ITCZ, *Geophys. Res. Lett.*, *43*, 2389–2395, doi:10.1002/2016GL068145.
Lynn, K. J. W., Y. Otsuka, and K. Shiokawa (2011), Simultaneous observations at Darwin of equatorial bubbles by ionosonde-based range/time displays and airglow imaging, *Geophys. Res. Lett.*, *38*, L23101, doi:10.1029/2011GL049856.
Mathews, J. D., and F. S. Bekeny (1979), Upper atmosphere tides and the vertical motion of ionospheric sporadic layers at Arecibo, *J. Geophys. Res.*, *84*, 2743–2750, doi:10.1029/JA084iA06p02743.
Patra, A. K. (2008), Some aspects of electrostatic coupling between E and F regions relevant to plasma irregularities: A review based on recent observations, *J. Atmos. Sol. Terr. Phys.*, *70*, 2159–2171, doi:10.1016/j.jastp.2008.05.013.
Patra, A. K., S. Sripathi, and D. Tiwari (2004), Coupling effect of the equatorial F region irregularities on the low latitude E region instability processes, *Geophys. Res. Lett.*, *31*, L17803, doi:10.1029/2004GL020486.
Patra, A. K., T. Yokoyama, M. Yamamoto, S. Saito, T. Maruyama, and S. Fukao (2005), Disruption of E region echoes observed by the EAR during the development phase of equatorial spread F: A manifestation of electrostatic field coupling, *Geophys. Res. Lett.*, *32*, L17104, doi:10.1029/2005GL022868.
Patra, A. K., A. Taori, P. P. Chaitanya, and S. Sripathi (2013), Direct detection of wavelike spatial structure at the bottom of the F region and its role on the formation of equatorial plasma bubble, *J. Geophys. Res. Space Physics*, *118*, 1196–1202, doi:10.1002/jgra.50148.
Picone, J. M., A. E. Hedin, D. P. Drob, and A. C. Aikin (2002), NRLMSISE-00 empirical model of the atmosphere: Statistical comparisons and scientific issues, *J. Geophys. Res.*, *107*(A12), 1468, doi:10.1029/2002JA009430.
Raizada, S., and H. S. S. Sinha (2000), Some new features of electron density irregularities over SHAR during strong spread F, *Ann. Geophys.*, *18*, 141–151, doi:10.1007/s00585-000-0141-8.
Roddy, P. A., G. D. Earle, C. M. Swenson, C. G. Carlson, and T. W. Bullett (2007), The composition and horizontal homogeneity of *E* region plasma layers, *J. Geophys. Res.*, *112*, A06312, doi:10.1029/2006JA011713.
Stephan, A. W., M. Colerico, M. Mendillo, B. W. Reinisch, and D. Anderson (2002), Suppression of equatorial spread *F* by sporadic *E*, *J. Geophys. Res.*, *107*(A2), 1021, doi:10.1029/2001JA000162.
Thampi, S. V., M. Yamamoto, R. T. Tsunoda, Y. Otsuka, T. Tsugawa, J. Uemoto, and M. Ishii (2009), First observations of large-scale wave structure and equatorial spread F using CERTO radio beacon on the C/NOFS satellite, *Geophys. Res. Lett.*, *36*, L18111, doi:10.1029/2009GL039887.
Tsunoda, R. T. (1983), On the generation and growth of equatorial backscatter plumes: 2. Structuring of the west walls of upwellings, *J. Geophys. Res.*, *88*, 4869–4874, doi:10.1029/JA088iA06p04869.
Tsunoda, R. T. (2008), Satellite traces: An ionogram signature for large-scale wave structure and a precursor for equatorial spread F, *Geophys. Res. Lett.*, *35*, L20110, doi:10.1029/2008GL035706.
Tsunoda, R. T. (2009), Multi-reflected echoes: Another ionogram signature of large-scale wave structure, *Geophys. Res. Lett.*, *36*, L01102, doi:10.1029/2008GL036221.
Tsunoda, R. T. (2015), Upwelling: A unit of disturbance in equatorial spread F, *Prog. Earth Planet. Sci.*, *2*, 9, doi:10.1186/s40645-015-0038-5.
Tsunoda, R. T., and W. L. Ecklund (2007), On the post-sunset rise of the equatorial *F* layer and superposed upwellings and bubbles, *Geophys. Res. Lett.*, *34*, L04101, doi:10.1029/2006GL028832.
Tsunoda, R. T., and B. R. White (1981), On the generation and growth of equatorial backscatter plumes: 1. Wave structure in the bottomside *F* layer, *J. Geophys. Res.*, *86*, 3610–3616, doi:10.1029/JA086iA05p03610.
Tsunoda, R. T., M. Yamamoto, T. Tsugawa, T. L. Hoang, S. Tulasi Ram, S. V. Thampi, H. D. Chau, and T. Nagatsuma (2011), On seeding, large-scale wave structure, equatorial spread *F*, and scintillations over Vietnam, *Geophys. Res. Lett.*, *38*, L20102, doi:10.1029/2011GL049173.
Tulasi Ram, S., M. Yamamoto, R. T. Tsunoda, S. V. Thampi, and S. Gurubaran (2012), On the application of differential phase measurements to study the zonal large scale wave structure (LSWS) in the ionospheric electron content, *Radio Sci.*, *47*, RS2001, doi:10.1029/2011RS004870.
Tulasi Ram, S., M. Yamamoto, R. T. Tsunoda, H. D. Chau, T. L. Hoang, B. Damtie, M. Wassaie, C. Y. Yatini, T. Manik, and T. Tsugawa (2014), Characteristics of large-scale wave structure observed from African and Southeast Asian longitudinal sectors, *J. Geophys. Res. Space Physics*, *119*, 2288–2297, doi:10.1002/2013JA019712.
Woodman, R. F., and C. LaHoz (1976), Radar observations of F region equatorial irregularities, *J. Geophys. Res.*, *81*, 5447–5466, doi:10.1029/JA081i031p05447.
Yokoyama, T., S. Fukao, and M. Yamamoto (2004), Relationship of the onset of equatorial *F* region irregularities with the sunset terminator observed with the Equatorial Atmosphere Radar, *Geophys. Res. Lett.*, *31*, L24804, doi:10.1029/2004GL021529.
Zalesak, S. T., and S. L. Ossakow (1980), Nonlinear equatorial spread F: Spatially large bubbles resulting from large horizontal scale initial perturbations, *J. Geophys. Res.*, *85*, 2131–2142, doi:10.1029/JA085iA05p02131.